Friction and shear fracture of an adhesive contact under torsion

Antoine Chateauminois,[*] Christian Fretigny, and Ludovic Olanier

Laboratoire de Physico-Chimie des Polymères et des Milieux Dispersés, UMR CNRS 7615, Ecole Supérieure de Physique et Chimie Industrielles (ESPCI), Paris, France

The shear failure or stiction of an adhesive contact between a poly(dimethylsiloxane) (PDMS) rubber and a glass lens has been investigated using a torsional contact configuration. As compared to linear sliding, torsion presents the advantage of inducing a shear failure under a pure mode III condition, while preserving the cylindrical symmetry of the contact. The surface of the transparent PDMS substrate was marked using a network of dots in order to monitor continuously the in-plane surface displacements during the stiction process. Using a previously developed inversion procedure (A. Chateauminois and C. Fretigny, Eur. Phys. J. E **27**, 221 (2008)), the corresponding surface shear stress distributions were obtained from the displacement fields. Stiction was found to involve the progressive shrinkage of a central adhesive zone surrounded by an annular microslip region. Adhesion effects were especially evidenced from a stress overshoot at the boundary of the adhesive zone. The experimental data were analysis using an extension to torsional contact of the Maugis-Dugdale approach's to adhesive contacts which takes into account frictional effects. This model allowed to extract an effective adhesion energy in the presence of friction, which dependence on kinetics effect is briefly discussed.

I. INTRODUCTION

The shear failure of an adhesive contact during the incipient stages of sliding friction is often refereed to as a stiction process [1–3]. Such mechanisms are encountered in many practical applications such as, for example, tire/road contacts or MEMs. They also pertain to the discontinuous stick-slip motions which are observed in many frictional systems. From a fundamental point of view, stiction involves a complex and poorly understood interplay between frictional energy dissipation and adhesion. At the macroscopic level, a static coefficient of friction is often ascribed to the onset of sliding which may differ significantly from the dynamic coefficient of friction measured under steady-state sliding. The underlying wisdom behind these static and dynamic friction concepts is that the onset of friction involves a sharp transition from a purely elastic state without any slip at the interface to a steady-state frictional situation. However, this assumption has long been recognized as an oversimplification.

The problem of the friction threshold was first addressed in the case of nonadhesive contacts. For Hertzian contacts, Mindlin's [4] and co-workers have early predicted that incipient sliding involves microslip processes well below the sliding threshold. Assuming that a local Coulomb's friction law holds within the frictional interface, Mindlin contact mechanics theory predicts that a microslip zone develops from the periphery of the circular contact when the lateral load is progressively applied. Since the seminal work by K.L. Johnson [5], this model has received many experimental confirmations from the observation of worn contacts produced by the application of small amplitude oscillating micromotions below the sliding threshold. More recently, some at-

tempts have been made by Bureau and co-workers [6] to extend the Mindlin's approach to multicontact interfaces between rough solid surfaces. Interestingly, this investigation especially raised the question of the relevance of a local Coulomb's friction law at the scale of microcontacts between individual asperities. The knowledge of the *local* friction law is in fact a key aspect in any description of the friction threshold, either in adhesive or in nonadhesive contacts. Unfortunately, this local friction law, i.e., the relationship between the actual local pressure and shear stress at the sliding interface, is rarely determined directly. Instead, it is usually inferred from the *macroscopic* friction law provided by the experimental relationship between the normal and lateral forces.

Although the propagation of microslip during incipient sliding is often described as a progressive mechanism, some recent studies by Rubinstein *et al.* [7,8] showed that it can also involve some more complex crack propagation mechanisms. From *in situ* observation of a rough extended interface between two glassy polymer blocks, these authors showed that the onset of motion upon the application of shear is preceded by a discrete sequence of crack like precursors, which are initiated at shear levels that are well below the threshold for static friction.

Stiction processes within adhesive contact between rubbers and spherical glass probes were first addressed experimentally by Barquins *et al.* [9,10]. In such a system, adhesion is governed by Van der Waals surface forces and an intimate contact between the two surfaces can be assumed to occur due to the low modulus of the rubber. Starting from the adhesive contact, as soon as a shear load is applied, the contact area becomes smaller and loses its circular symmetry with a marked shrinkage of the trailing edge which occurs by a peeling process due to the existence of high tensile stresses at the rear. In addition, microslip also takes place in an annular zone adjacent to the edge of the contact similarly to the nonadhesive behavior described by Mindlin. In other words,

---
*[*]antoine.chateauminois@espci.fr; http://www.espci.fr/usr/chateau/

the failure of adhesion involves a rather complex combination of tensile (i.e., peeling) and interface shear modes. These processes can be considered from a fracture mechanics point of view where the boundary of the adhesion zone is assimilated to a propagating crack. A fundamental question is then to determine from the experiments the adhesion energy which rules the dynamics of crack propagation and its interplay with friction. The approach is through fracture mechanics concepts in which the rate of elastic strain energy is equated to the work done against surface forces both frictional and adhesive. Some models along these guidelines were proposed by Savkoor [11,12] and Johnson [13] with the assumption of a constant frictional shear stress within the microslip zone. Johnson's theory especially incorporates in a refined manner a possible interaction between normal adhesive forces and tangential friction forces at the periphery of the contact. A reasonable agreement is found with Barquins' [10] and Savkoor's [12] experimental results for the peeling of the contact when a lateral force is applied. However, the possible role played by adhesion during the shear failure of the contact interface, i.e., microslip propagation, is more controversial. It is especially not clear how the surface force field acting at the periphery of the adhesive zone can affect the separation of contacting points at the interface. In the models by Savkoor and Johnson, this is reflected by the different hypothesis regarding shear stress distribution at the boundary between adhesive and frictional zone. In this paper, we have investigated stiction processes of an adhesive contact between a silicone rubber and a glass spherical probe using an approach which incorporates two original features (i) the use of a torsional contact configuration instead of the classical linear friction experiment (ii) the determination of the actual shear stress distribution at the surface of the rubber substrate from a measurement of the surface displacement field using a methodology previously validated for steady-state linear sliding contacts [14].

As compared to linear sliding conditions, torsional contacts present the advantage of preserving the cylindrical symmetry of the contact. Moreover, the shear failure of the interface occurs in a more simple "antiplane" shear mode (denoted to as Mode III in the fracture mechanics terminology), whereas linear sliding involves a combination of Mode III and "in-plane" (Mode II) shear modes.

The first experimental investigation using a torsional contact configuration was carried out by Hetenyi and Mc Donald [15]. Using a set of careful photoelastic measurements, these authors were able to get some insight into the contact stress distribution when complete slip occurs. The objective of this study was essentially to validate contact mechanics models developed by Lubkin [16] and Mindlin's and co-workers [4,17] under the assumption of a local Coulomb's friction law. Such contact mechanics approaches were later extended to the torsion of viscoelastic spheres in contact by Dintwa and co-workers [18,19]. Torsional contact situations have also been used with soft materials with the objective of investigating contact instabilities under full sliding conditions. In an early study using a rubber/glass contact, Barquins [20] especially examined the occurrence detachment waves reminiscent to Schallamach waves, the so-called "interfaceons." More recent studies by Chaudhury and co-workers [21] also

focused on other contact instabilities induced within a torsional contact between a mechanically confined silicone film and a flat ended cylindrical punch.

Contact imaging approaches combined with correlation methods have been used by a few authors in order to monitor stiction mechanisms within glass/rubber contacts under linear sliding conditions [22–25]. Light scattering from the interface between a glass surface and a poly(dimethylsiloxane) (PDMS) substrate microstructured with pyramids was also used by Bennewitz and co-workers in order to measure friction induced strains [26]. In the present torsional contact investigation, the measurement of the surface displacement field is intended to provide information about the dynamics of the shrinkage of the adhesive zone when the twisting motion is applied. In addition, the determination of the surface shear stress distribution from the inversion of the displacement field provides insights into the local friction law within microslip zone and the stress state at the boundary between the adhesion and microslip zones. This allows to clarify the role played by adhesion in the stiction process.

In the first part of the paper, experimental results are reported regarding displacement and stress fields during stiction and steady-state friction. In a second section, a torsional contact model is introduced which accounts for adhesion, using the guidelines of the so-called Maugis-Dugdale adhesive contact model [27,28]. In a last section, results are analyzed in the light of this model. From the measurement of the radius of the adhesive zone, apparent adhesion energy in the presence of friction is especially obtained which dependence on the applied angular velocity is briefly discussed.

II. EXPERIMENTAL RESULTS

A. Experimental details

A commercially available transparent PDMS silicone (Sylgard 184, Dow Corning, Midland, MI) is used as an elastomer substrate. In order to monitor contact induced surface displacements, a square network of small cylindrical holes (diameter 8 μm, depth 11 μm and center-to-center spacing 40 μm) is produced on the PDMS surface by means of conventional microlithography techniques. Under transmitted light observation conditions, this pattern appears as a network of dark spots which are easily detected using image analysis. In order to elaborate these marked PDMS surfaces, a resin template with a network of cylindrical pillars is first realized on a silicon wafer by means of soft microlithography. The reactive silicon mixture in stoichiometric proportions (10:1 by weight) is then directly molded onto this template and cured in an oven at 50 °C for 48 h. Specimen size ($15 \times 60 \times 60$ mm^3) ensures that semi-infinite contact conditions are achieved during torsion experiments (i.e., the ratio of the substrate thickness to the contact radius is greater than ten [29]). Before use, PDMS specimens are thoroughly washed with isopropanol and subsequently dried under vacuum.

Millimeter sized contacts are achieved between the PDMS substrate and a planoconvex BK7 glass lens (Melles Griott, France) with a radius of curvature of 14.8 mm. In order to avoid stick slip during friction, the glass surface is
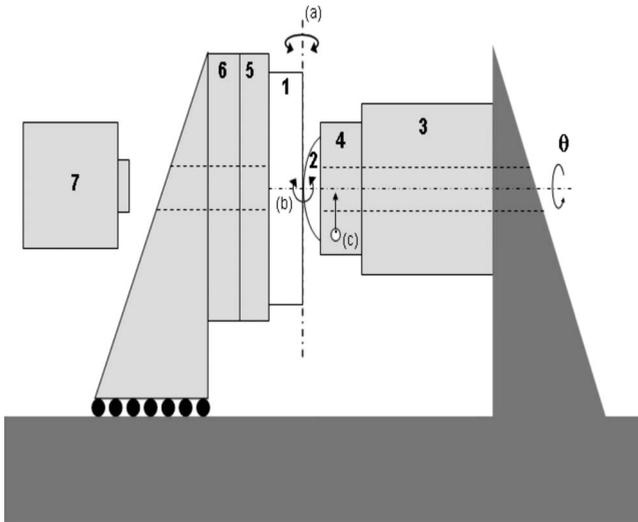
FIG. 1. Schematic description of the torsional contact apparatus. A normal contact is achieved between a flat PMDS specimen (1) and a planoconvex glass lens (2). The glass lens is twisted at imposed angular velocity, $\dot{\theta}$, by means of a rotary stage (3). The alignment of the apex of the lens with respect to the axis of rotation of the stage (c) is allowed by a XY translation stage (4). A set of two goniometric stages (5) and (6) is used to ensure that the PDMS surface is perpendicular to the axis of rotation. The corresponding rotation axis (a) and (b) are perpendicular and cross each other at the contact point. Contact images are recorded through the transparent PDMS specimen by means of a zoom and a CCD camera (7).

treated with perfluorodecyltrichlorosilane. The hydrozilation reaction is carried out by evaporating the silane under gentle vacuum (0.5 mbar) for one night at room temperature. Just before exposure to the evaporated silane, the surface of the glass lens is activated in a water vapor plasma.

Contact torsion experiments are carried out using a homemade device depicted in Fig. 1. Normal contact is achieved by means of a linear displacement stage under imposed displacement conditions. During experiments, the glass lens is rotated at imposed angular velocity (between 0.01 and 1 deg s^{-1}) using a motorized rotation stage (MPD-3, Polytech PI, Germany). Before twisting the lens, a contact dwell time of one hour is systematically observed in order to allow for the development of adhesion. During torsion, images of the deformed contact zone are continuously recorded through the transparent PDMS substrate using a zoom and a charge-coupled device (CCD) camera. The system is configured to a frame size of (1024 × 1024) pixels with 8 bits resolution. Images are acquired at a frequency ranging from 0.01 to 12 Hz. The twist angle corresponding to each image is deduced from a reading of the parity conserving system clock after checking that the prescribed angular velocity is actually achieved. Subpixel detection of individual dots on the PMDS surface is carried out with good accuracy using image processing.

As pointed out in a previous study [30], sliding paths under torsional contact conditions are critically dependent on alignment problems. In order to get a reliable axisymmetric displacement field, it was found necessary (i) to align accurately the apex of the glass lens with respect to the axis of
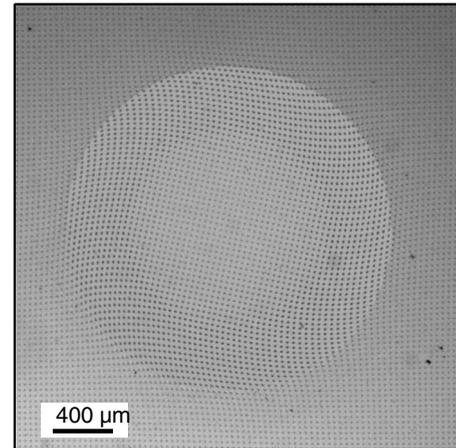
FIG. 2. Image of a twisted contact during stiction.

rotation of the stage (ii) to ensure that the axis of rotation of the lens is perfectly perpendicular with respect to the PDMS surface. The first requirement is achieved using a XY translation stage located in between the glass lens holder and the rotary stage. The position of this stage is progressively adjusted using an iterative procedure until no substantial translation of the contact area (within less than 20 μm) is observed during rotation of the glass lens. A set of two goniometric stages located below the PDMS specimen holder is used to fulfill the second requirement. The location of these stages ensures that their axes of rotation are perpendicular and cross each other at the contact point. Then, two independent rotation axes are available to tilt the PDMS surface with respect to the lens. The alignment procedure consists in ensuring that the measured center of rotation (see below for details) matches the center of the contact area within less than 20 μm. The corresponding residual alignment error of the normal to the specimen surface with respect to the axis of rotation was less than 2 mrad.

B. Displacement fields

As an example, an image of the contact zone taken during the stiction process is shown in Fig. 2. From the distortion of the surface dots pattern, the partition of the contact area into a central adhesive zone characterized by a rigid body rotation and an outer slip region is clearly identified. Within experimental accuracy, no change in the size of the contact was detected during the whole stiction process. From acquired images, the displacement of each dot at the surface of the PDMS surface can easily be monitored as function of the twist angle. Then, each contact image produces a set of about 12 500 data points where in-plane displacements are measured using Cartesian coordinates. Owing to the symmetry of the contact, it is, however, more appropriate to describe displacements using their cylindrical components. This requires that the center of rotation is known accurately. The latter was determined from the location within the contact where the magnitude of the measured displacement is minimized. At this point, the measured residual displacement was found to be less than 3 μm, i.e., less than 2% of the maximum displacement.
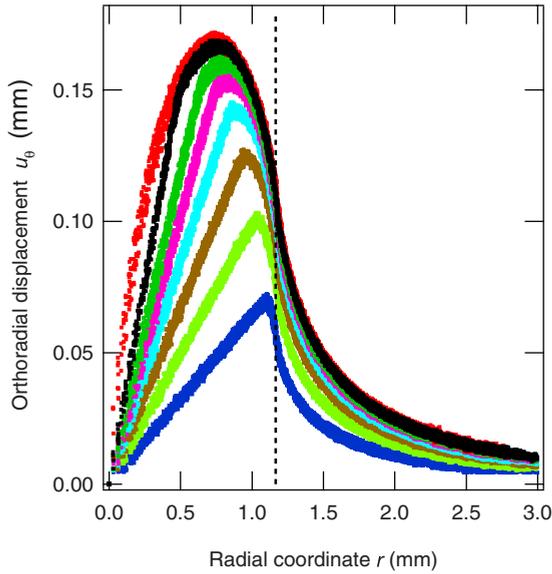
FIG. 3. (Color online) Measured orthoradial displacement as a function of the contact radial coordinate and of the applied angle of twist ($\dot{\theta}$=0.1 deg s^{-1}). The dotted line delimits the contact area. Applied twist angles from bottom to top: θ=0.065, 0.10, 0.13, 0.17, 0.20, 0.24, and 0.31 rad.

Figure 3 shows an example of the measured orthoradial surface displacement, u_θ, as a function of the radial coordinate at various stages of the stiction process. The scatter in the data points mostly reflects some residual imperfection in the alignment of the torsion device. This was evidenced by a small (less than 10 μm) angular variation in the orthoradial displacements measured at a given point.

Within experimental errors, the radial displacement component, u_r, was found negligible. During stiction (i.e., for θ less than about 0.5 rad), the partition of the contact zone in an inner adhesive zone (where u_θ depends linearly on the radial coordinate r) and an external microslip zone is clearly seen.

Figure 4 shows orthoradial displacements normalized with respect to the radial coordinate as a function of the twist angle. The various plots correspond to a selection of surface points located within the contact area and distributed along its radius. In such a representation, the normalized orthoradial displacement follows a straight line with unit slope as long as the considered surface point stays in the adhesive zone. Then, transition from the adhesive to the steady-state frictional state is indicated by a departure from this linear behavior. An alternate and maybe more precise description of the transition from the adhesive to the frictional state is provided by the measurement of the actual sliding velocity, v, at every location within the contact interface. The latter can be determined from the measured orthoradial displacement according to the following expression:

$$v = r\dot{\theta} - \dot{u_\theta}, \tag{1}$$

where r is the radial coordinate and $\dot{\theta}$ the imposed angular velocity.
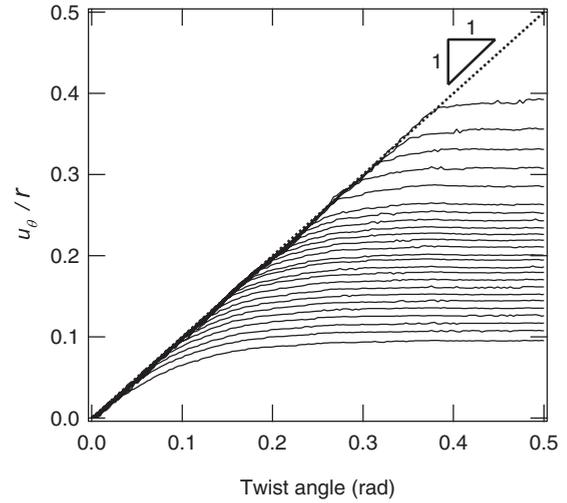
FIG. 4. Orthoradial displacement, u_θ, normalized with respect to the radial coordinate, r, as a function of the applied twist angle ($\dot{\theta}$ =0.1 deg s^{-1}). The different curves correspond to different locations within the contact area from r/a=0.29 (top) to r/a=0.97 (bottom), where a is the contact radius.

Figure 5 shows the corresponding measurement for a set of contact points regularly distributed along the radial coordinate. For each of the considered locations, a very steep transition is observed from the adhesive state (i.e., from a vanishing sliding velocity) to steady-state friction (i.e., v =$r\dot{\theta}$). From the corresponding sliding threshold, the radius, c, of the adhesive zone can be accurately determined as a function of the applied twist angle. Results are reported in Fig. 6 for three different imposed velocities. It is clearly seen that the shrinkage of the adhesive zone is delayed when the angular velocity is increased. If the boundary between the adhesive and the friction zones is assimilated to a fracture, this velocity dependence may be viewed as evidence of the occurrence of dissipative processes at the crack tip. This hy-
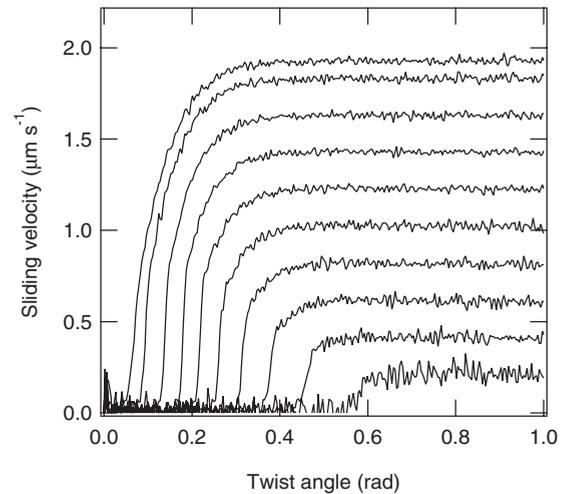
FIG. 5. Actual sliding velocity as a function of the applied twist angle for different locations within the contact ($\dot{\theta}$=0.1 deg s^{-1}). From bottom to top: r/a=0.2, 0.3, 0.4, 0.5, 0.6, 0.7, 0.8, 0.9 and 0.95.
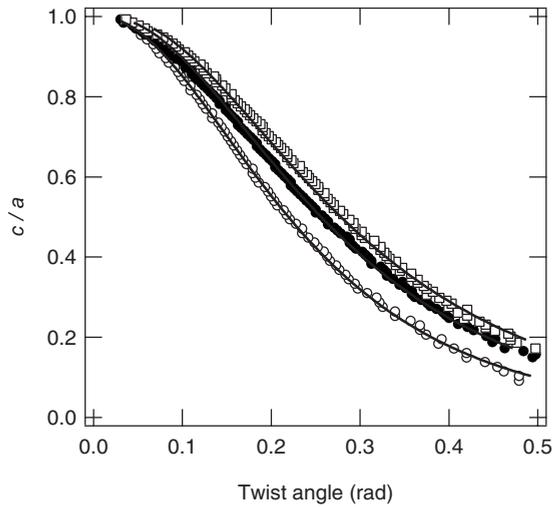
FIG. 6. Normalized radius of the adhesive zone, c/a, as a function of the twist angle for different applied angular velocities. ($\bigcirc$) $\dot{\theta} = 0.01$ deg s^{-1}, ($\bullet$) $\dot{\theta} = 0.1$ deg s^{-1}, and ($\square$) $\dot{\theta} = 1$ deg s^{-1}. Solid lines correspond to a fit to Eq. (29) (see text for details).

pothesis is consistent with the observation of a steep velocity gradient at the transition from the adhesive to the frictional state. Accordingly, high strain rates can be locally achieved within the PDMS substrate which could result in some localized viscoelastic dissipation at the crack tip.

C. Shear stress fields

From the experimental displacement field, surface shear stress distribution can be deduced using the inversion procedure detailed in [14]. The basis for this inversion is the so-called Green's tensor which provides the expressions for the displacements induced within a semi-infinite elastic body by a point loading applied to the surface [31]. If the expressions for point loading are extended to a distribution of surface tractions, it comes out that the lateral surface displacement field can be expressed as a convolution of the surface shear stresses by the so-called Green's functions which are known analytically and depend only on the material modulus and on the space coordinates. As detailed in [14], a Van Cittert iterative deconvolution procedure was implemented in order to get the surface shear stress from the measured in-plane displacements. In this analysis, displacement and interfacial stresses are described using their Cartesian components. For the purpose of inversion, interpolated displacement fields in Cartesian coordinates were thus generated from the experimental displacement profiles. As mentioned above, the measured radial displacement is negligible and only the orthoradial displacement component is thus used to generate the displacement field in Cartesian coordinate. Typical orthoradial shear stress distributions are shown in Fig. 7 at various stages of the stiction process. Under steady-state sliding [Fig. 7(g)], a nearly constant interface shear stress is obtained everywhere at the interface, except at the vicinity of the center of the contact. From clear symmetry reasons, one cannot expect the orthoradial shear stress not to be zero at the center
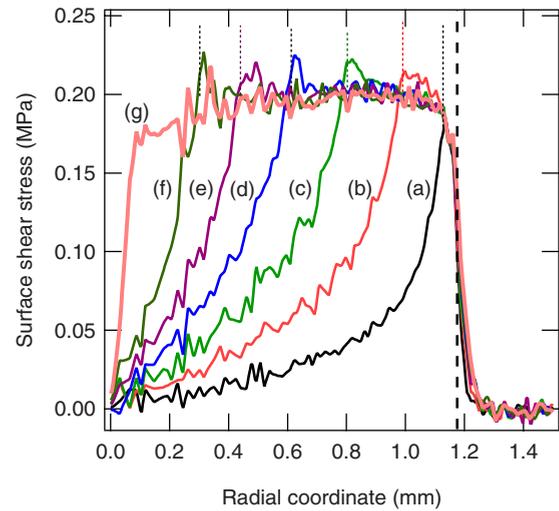
FIG. 7. (Color online) Orthoradial surface shear stress profiles obtained form the inversion of the measured surface displacement field at different stages of the stiction process ($\dot{\theta} = 0.1$ deg s^{-1}). (a) $\theta = 0.068$ rad, (b) $\theta = 0.14$ rad, (c) $\theta = 0.21$ rad, (d) $\theta = 0.28$ rad, (e) $\theta = 0.35$ rad, (f) $\theta = 0.43$ rad, and (g) steady-state friction. The large dotted line delimits the contact zone. Small dotted lines indicate the locations of the adhesive zone as it is determined independently from Fig. 6.

of the twisting contact. A discussion of this small radii effect is left to the discussion section.

The observation that the steady-state shear stress is roughly constant within the contact—except at the center of the contact—suggests that friction between PDMS and a smooth glass surface is not very sensitive to sliding velocity. The velocity dependence of the steady-state frictional shear stress is further examined by plotting the values of $\tau_{\theta z}$ as a function of the local sliding velocity. If the regions close to the center of the contact (i.e., $r < 100$ μm) are discarded, it comes out that all the shear stress data merge onto a single master curve when the applied angular velocity is varied from 0.01 to 1 deg s^{-1} (Fig. 8). Over about three decades, the frictional shear stress exhibits a weak logarithmic dependence on the sliding velocity which is consistent with previous observations for similar systems [14].

During stiction (i.e., for θ less than about 0.45 rad), a stress overshoot is observed at the boundary between the adhesive and the microslip zones [Fig. 7(a)–7(f)]. Although the actual shape of this stress peak is certainly affected by the iterative deconvolution operation involved in the inversion algorithm, it clearly pertains to adhesion effects. Indeed, classical model for the stiction of nonadhesive contact [4,17] do not predict any stress overshoot at the boundary of the stick zone. In the contact model developed below, the assumption of a stress difference between the edge of the adhesive zone and the surrounding microslip annulus is the key element to account for adhesion.

III. TORSIONAL CONTACT MODEL

A. Formulation of the contact problem

For a contact between a rigid sphere on an incompressible (Poisson's ratio $\mu = 0.5$) semi-infinite substrate, normal, and
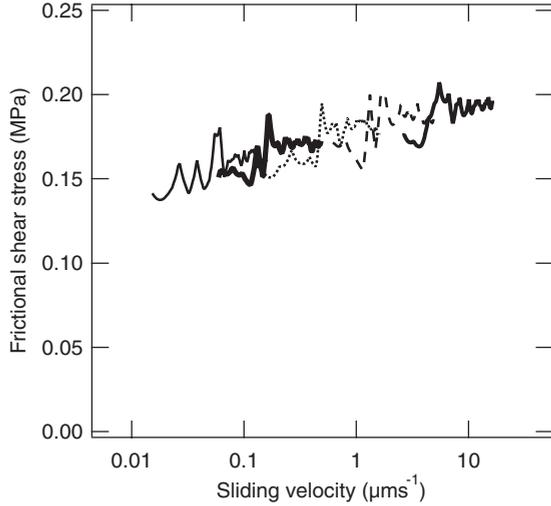
FIG. 8. Steady-state shear stress as a function of the actual sliding velocity at the contact interface. Solid line: $\dot{\theta}=0.01$ deg s^{-1}, thick solid line: $\dot{\theta}=0.03$ deg s^{-1}, small dotted line: $\dot{\theta}=0.1$ deg s^{-1}, large dotted line: $\dot{\theta}=0.3$ deg s^{-1} medium solid line: $\dot{\theta}=1$ deg s^{-1}

tangential loadings are decoupled [32,33] which implies that the experiment can be described into a normal indentation problem on one hand and a purely tangential problem on the other hand. This decomposition holds when the contact boundary conditions are given in terms of stress or strain at the surface. The adhesive contact may be more complex as discussed in Refs. [13,34]. This aspect is not discussed in this section where the mechanisms of adhesion break are not discussed. Jäger [35] derived the mechanical behavior of axisymmetric bodies of equal material in contact under torsion by using a superposition of adhering cylinders in rotation. Though this derivation was explicitly made for a couple of identical materials, it remains correct in the case of an undeformable punch on an incompressible material [32,33]. Then, following [35], one introduce a continuous superposition of adhering coaxial cylinders with radii α less than a the contact radius. The function $h(\alpha)$ describes the way they are twisted: cylinders which radii are comprised between α and $\alpha+d\alpha$ are twisted by an angle $h(\alpha)d\alpha$. The interfacial stress $\sigma_{\theta z}$ induced by a twisted flat-end punch in contact with a half-space under complete adhesion is

$$\sigma_{\theta z}(r) = \frac{4\mu}{\pi} \frac{\varphi r}{\sqrt{\alpha^2 - r^2}}, \tag{2}$$

$$\sigma_{rz}(r) = 0, \tag{3}$$

and that the surface displacement field is

$$u_\theta(r) = \begin{cases} \varphi r & \text{for } r \le \alpha \\ \dfrac{2}{\pi} \varphi r \left[\sin^{-1}\dfrac{\alpha}{r} - \dfrac{\alpha}{r}\sqrt{1 - \alpha^2/r^2} \right] & \text{for } r \ge \alpha \end{cases}, \tag{4}$$

$$u_r(r) = u_z(r) = 0. \tag{5}$$

α is the cylinder radius, φ is the twist angle and μ is the shear modulus. The stress corresponding to the superposition can be written as

$$\sigma_{\theta z}(r) = \frac{4\mu r}{\pi} \int_r^a \frac{h(\alpha)}{\sqrt{\alpha^2 - r^2}} d\alpha. \tag{6}$$

(At a radial distance r from the axis, the only cylinders with a radius $\alpha > r$ contribute to the stress field). In the same way, the displacement can be expressed as:

$$u_\theta(r) = \int_0^r \frac{2}{\pi} \left[r \sin^{-1}\frac{\alpha}{r} - \alpha\sqrt{1 - \alpha^2/r^2} \right] h(\alpha) d\alpha$$

$$+ \int_r^a r h(\alpha) d\alpha. \tag{7}$$

After integration by parts of the first integral, we obtain

$$u_\theta(r) = -\frac{4}{\pi r} \int_0^r \frac{\alpha^2 H(\alpha)}{\sqrt{r^2 - \alpha^2}} d\alpha, \tag{8}$$

where $H(\alpha)$ is the antiderivative of $h(\alpha)$ with $H(a)=0$. Equations (6) and (8) can be inverted using the Abel integral equation

$$h(\alpha) = -\frac{1}{2\mu} \frac{d}{d\alpha} \int_\alpha^a \frac{\sigma_{\theta z}(r)}{\sqrt{r^2 - \alpha^2}} dr, \tag{9}$$

$$H(\alpha) = -\frac{1}{2\alpha^2} \frac{d}{d\alpha} \int_0^\alpha \frac{r^2 u_\theta(r)}{\sqrt{\alpha^2 - r^2}} dr. \tag{10}$$

Note that Eq. (9) can be written as

$$H(\alpha) = -\frac{1}{2\mu} \int_\alpha^a \frac{\sigma_{\theta z}(r)}{\sqrt{r^2 - \alpha^2}} dr \tag{11}$$

One may notice that if it is assumed that stress does not diverge, Eq. (11) implies that $H(\alpha)$ is continuous. This continuity condition will be used at different stages of the calculation. In the following, expressions (6), (8), (10), and (11) are used to describe several friction situations, in a way similar to other calculations developed for normal loading problems [35–38].

B. Nonadhesive stiction

During the stiction, orthoradial displacements are prescribed within a disk of radius c (the stick region) while the interfacial stress are prescribed in the outer region ($c < r < a$, sliding region). Then, $H(\alpha)$ can be totally defined from Eqs. (10) and (11). In turn, stresses in the inner region and displacements in the outer one (and even out of the contact area) are obtained from Eqs. (6) and (8). In some respects, this description is similar to the adhesive contact of Maugis-Dugdale [27,37–39]. More precisely, in the stick region, $u_\theta = \theta r$, where θ denotes the torsion angle. Then, defining $H_<(\alpha)$ and $H_>(\alpha)$, respectively, as the values of $H(\alpha)$ in the

stick region and in the outer annulus. From Eq. (10), one obtains $H_<(\alpha) = -\theta$. For $\alpha > c$, Eq. (11) reads

$$H_>(\alpha) = -\frac{1}{2\mu}\int_\alpha^a \frac{\sigma_{\theta z}(r)}{\sqrt{r^2 - \alpha^2}}dr.$$

The nondivergence of stresses at $r = c$, imposes $H_<(c) = H_>(c)$, or

$$\theta = \frac{1}{2\mu}\int_c^a \frac{\sigma_{\theta z}(r)}{\sqrt{r^2 - c^2}}dr, \tag{12}$$

which determines the stick radius, c, if the interfacial stresses are given. Two different situations are analyzed below.

1. Local Coulomb's friction law

For a Coulomb sliding friction model, with coefficient of friction, f, the orthoradial surface stress is

$$\sigma_{\theta z}(r) = f\sigma_{zz} = \frac{3fP}{2\pi a^3}\sqrt{a^2 - r^2}, \tag{13}$$

where P is the normal load of the Hertzian contact. For $c < r < a$, one get

$$H_>(\alpha) = -\frac{3fP}{4\pi\mu a^2}r\left[K\left(\sqrt{1 - \frac{\alpha^2}{a^2}}\right) - E\left(\sqrt{1 - \frac{\alpha^2}{a^2}}\right)\right], \tag{14}$$

where K and E are the complete elliptic integrals of first and second kind. For a given torsion angle, the stick boundary radius c can be deduced from the nondivergence condition, which reads

$$\theta = \frac{3fP}{4\pi\mu a^2}\left[K\left(\sqrt{1 - \frac{c^2}{a^2}}\right) - E\left(\sqrt{1 - \frac{c^2}{a^2}}\right)\right]. \tag{15}$$

This expression is identical to that proposed in Ref. [18]. It can be noted that, for arbitrary large torsion angles, the size of the stick domain remains finite in this model. This nonphysical effect has been systematically overlooked in previous torsional contact mechanics theories [15–17,40] and will be discussed in the discussion section.

2. Constant friction stress model

We have recently shown that for a smooth glass sphere sliding on PDMS, the local friction stress is nearly constant in the contact area [14]. For this friction law, $\sigma_{\theta z} = \tau_0$,

$$H_>(\alpha) = -\frac{\tau_0}{2\mu}\cosh^{-1}\frac{a}{\alpha}, \tag{16}$$

we obtain the nondiverging condition at a torsion angle θ from Eq. (12)

$$\cosh\frac{2\theta\mu}{\tau_0} = \frac{a}{c}. \tag{17}$$

As for the Coulomb model discussed above, the torsion angle may increase indefinitely while the stick region conserves a finite radius.

C. Adhesive stiction

Adhesion in contact mechanics has been the subject of numerous studies. For the normal loading case, the interfacial forces responsible for adhesion have been described in several ways, giving rise to different models according to the mechanical properties of the involved materials, adhesion forces, applied load, and indenter curvature. Finally, a unified model is now available [27,39] which uses the so-called Dugdale crack model. In this description, the interfacial forces are supposed to be constant up to a given separation distance between the surfaces. Though rather rough, this model capture the essential features of the adhesive contact, as more realistic interfacial laws do not modify substantially the obtained results [38]. In the following, a variant of this model is adapted for the twist experiment: interfacial orthoradial tractions just beyond the stick region are supposed to be constant up to a radius which corresponds to a given orthoradial separation between points on both surfaces. Such an annulus corresponds to the Dugdale region. It is assumed that two small regions which were initially superimposed in the stick region are subjected to an orthoradial stress τ_D as long as their relative separation remains lower than a given distance Δ, i.e., when their radius is $c < r < c^*$. Beyond this radius, for $c^* < r < a$, a prescribed friction law accounts for the "free" sliding region stresses. The external radius for the Dugdale annulus, c^*, must be determined self-consistently. In the following, to be more explicit, a constant friction is assumed in the sliding region; this assumption is also consistent with the experimental observation of a weak dependence of the friction stress within the velocity gradient of the contact zone.

In the stick region ($r < c$), as above, $H(\alpha) = H_<(\alpha) = -\theta$. When $c^* < \alpha < a$, Eq. (16) holds

$$H(\alpha) \equiv H_>^+(\alpha) = -\frac{\alpha_0}{2}\cosh^{-1}\frac{a}{\alpha}, \tag{18}$$

and, for $c < \alpha < c^*$, $H(\alpha) \equiv H_>^-(\alpha)$ with

$$H_>^-(\alpha) = -\frac{1}{2\mu}\left[\tau_D\int_\alpha^{c^*}\frac{dr}{\sqrt{r^2 - \alpha^2}} + \tau_0\int_{c^*}^a\frac{dr}{\sqrt{r^2 - \alpha^2}}\right], \tag{19}$$

$$= -\frac{1}{2}\left[(\alpha_D - \alpha_0)\cosh^{-1}\frac{c^*}{\alpha} + \alpha_0\cosh^{-1}\frac{a}{\alpha}\right], \tag{20}$$

where the notations $\alpha_D = \tau_D/\mu$ and $\alpha_0 = \tau_0/\mu$ are used. The nondivergence condition at $r = c$ Eq. (12) reads

$$2\theta = (\alpha_D - \alpha_0)\cosh^{-1}\frac{c^*}{c} + \alpha_0\cosh^{-1}\frac{a}{c}. \tag{21}$$

Continuity condition for H at $\alpha = c^*$ is automatically fulfilled. The value of c^* is determined by expressing the condition that the orthoradial displacement reaches the Dugdale limit at this radius

$$\Delta = \theta c^* - u_\theta(c^*). \tag{22}$$

By extending the definition of $H_<(\alpha) = -\theta$ for $c < \alpha < c^*$, the following identity holds

$$\theta c^* = -\frac{4}{\pi c^*} \int_0^{c^*} \frac{\alpha^2 H_<(\alpha)}{\sqrt{c^{*2} - \alpha^2}} d\alpha. \qquad (23)$$

Then, one can express Eq. (22) as

$$\Delta = -\frac{4}{\pi c^*} \int_0^{c^*} \frac{\alpha^2 H_<(\alpha)}{\sqrt{c^{*2} - \alpha^2}} d\alpha + \frac{4}{\pi c^*} \int_0^{c} \frac{\alpha^2 H_<(\alpha)}{\sqrt{c^{*2} - \alpha^2}} d\alpha$$

$$+ \frac{4}{\pi c^*} \int_c^{c^*} \frac{\alpha^2 H_>(\alpha)}{\sqrt{c^{*2} - \alpha^2}} d\alpha, \qquad (24)$$

$$\Delta = \frac{4}{\pi c^*} \int_c^{c^*} \frac{\alpha^2 d\alpha}{\sqrt{c^{*2} - \alpha^2}} [H_>(\alpha) - H_<(\alpha)]. \qquad (25)$$

This expression together with the nondivergence condition (21) allows to express the solution of the Dugdale-friction problem, as c and c^* are obtained from these two equations. By denoting $c^* = c \cosh z$, Eq. (21) reads

$$z = \frac{2\theta - \alpha_0 \cosh^{-1} \dfrac{a}{c}}{\alpha_D - \alpha_0}. \qquad (26)$$

Then, from the variable change $\alpha \cosh zu = c^*$, Eq. (24) can be written as:

$$\Delta = \frac{2}{\pi} cz \cosh z \int_0^1 \frac{du}{\cosh^3 zu}$$

$$\times \left[2\theta(1-u) + \alpha_0 \left(u \cosh^{-1} \frac{a}{c} - \cosh^{-1} \frac{a \cosh zu}{c \cosh z} \right) \right]. \qquad (27)$$

In principle, the previous equation is sufficient to describe the adhesive stiction state as it couples the stick radius, the contact radius, the torsion angle, the elastic modulus, the friction stress, and the Dugdale stress and length. However it is rather difficult to analyze directly. In the following we will assume that the interfacial stress in the Dugdale region is much larger than the friction stress ($\alpha_D \gg \alpha_0$) and much larger than the shear modulus ($\alpha_D \gg 1$). Then, $z \ll 1$, and a first order z expansion of the previous equation leads to the relation

$$\left(2\theta - \alpha_0 \cosh^{-1} \frac{a}{c} \right)^2 = \frac{\pi}{c} \Delta \alpha_D. \qquad (28)$$

In this expression, $\Delta \alpha_D = \Delta \tau_D / \mu$ is *a priori* unknown, as it depends on the details of the crack mechanism. In the Dugdale description for mode I crack, $\Delta \tau_D$ would be identified as the reversible thermodynamic work of adhesion. The situation is less clear for the mode III, as friction plays a role in the crack mechanism. In the following, we will use the notation $\Gamma = \Delta \tau_D$ and interpret Γ as some effective adhesion energy,

$$2\theta - \alpha_0 \cosh^{-1} \frac{a}{c} = \sqrt{\frac{\pi \Gamma}{\mu c}}. \qquad (29)$$

When $\Delta = 0$, this equation corresponds to the non-adhesive friction case Eq. (17).

The above description of the stiction may apply when the rotation angle is not too small in order that a nonzero part of the contact area is in slip region (the Dugdale region does not touch the edge of the contact), i.e., above a critical angle θ^* for which the extremity of the Dugdale region corresponds to the contact edge. This regime can be considered as the limit of the previous one for $c^* = a$. One obtains

$$2\theta^* = \alpha_D \cosh^{-1} \frac{a}{c}, \qquad (30)$$

$$\theta^* = \sqrt{\frac{\pi \Gamma}{4 \mu a}}, \qquad (31)$$

which clearly states that adhesion results in the presence of a sliding threshold when the lens is twisted. From the above analysis, orthoradial stress distribution can be deduced from Eq. (6). This derivation is presented in Appendix A. It is also shown that the model can be described as a mode III crack problem, in the limit of a vanishing Dugdale region but with a finite effective adhesion energy. The first order expansion in the z parameter appears to be similar to the recovery of the JKR approximation in the Maugis-Dugdale description of adhesion [27].

IV. DISCUSSION

The above description of torsional friction is based on linear elasticity under a small deformation assumption. From Fig. 3 it is clear, however, that in-plane shear stress can be quite non-negligible at the periphery of the contact (about 40% at the contact edge). Though such strains are clearly out of the linear response of the PDMS [41], it is likely that because the highly strained region is rather localized, results of the model can be used (at least on a semiquantitative way) to interpret the experimental data. It can be stressed that this limitation in the model due to the small strain hypothesis is not specific to the torsional contact configuration. Most of the adhesive models for normal contacts also rely on a small strain-linear elasticity hypothesis, while high strains are also experimentally achieved at the contact edge during adhesion experiments with rubbers.

Another difficulty comes from the kinetics effects evidenced during the shrinkage of the adhesive zone: Fig. 6 indeed shows that stiction process depends on the applied angular velocity. In the theoretical description, however, no time dependent terms are introduced. In principle, a velocity dependent friction stress (such as this shown in Fig. 8) should be included in the model in order to describe friction in the outer microslip annulus. However, such a model improvement would imply considerable complication in the calculation since the problem now needs to be self-consistently solved. Nevertheless, the velocity dependence of the interfacial stress is rather weak (Fig. 8)—it can be con-
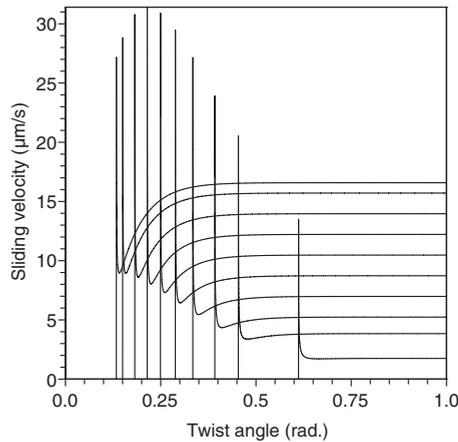
FIG. 9. Calculated sliding velocities at various locations along the contact radius as a function of the applied twist angle. The parameters ($a=1.165$ mm, $\tau_0=0.18$ MPa, $\mu=0.5$ MPa, and $\Gamma=130$ mJ m^{-2}) were selected in order to match as closely as possible the experimental conditions corresponding to Fig. 5. The normalized radial coordinates, r/a, corresponding to the different curves are the same as in Fig. 5.

FIG. 10. Shear stress distribution obtained from the iterative deconvolution of a calculated orthoradial displacement field. The displacement field was generated by the convolution of a constant shear stress distribution ($\sigma_{\theta z}=0.2$ MPa, dotted line) by the Green's functions. The initial value of the shear stress is not retrieved at the center of the contact as a result of the cut-off frequency of the deconvolution operation.

sidered as almost constant in most of the sliding region with a good approximation. However, this is probably not the case near the boundary of the stick region. Figure 9 shows the interfacial sliding velocity predicted by the model (see Appendix B for details on the calculation) for rather plausible experimental conditions. It is observed that, near the edge of the stick region, a velocity peak is expected. The high friction value in this region may substantially modify the stiction phase.

In addition, potential viscoelastic dissipation within the PDMS substrate is not taken into account, which may also introduce kinetics effects. The used PDMS substrate is a highly elastic elastomer with a loss factor, tan δ, less than 0.05 at 1 Hz at room temperature. As a consequence, viscoelastic dissipation may be assumed to be localized at the edge of the adhesive zone where the highest strains and strain rates are achieved. For the description of normal adhesion failure in situations where viscoelastic dissipation is localized at the edge of the adhesive zone, it has been proposed to use a crack velocity dependent adhesion energy [42,43]. By introducing the same phenomenological ansatz in the presented model, one can obtain a reasonably good agreement between the model and experimental data presented in Fig. 6. Values for the effective adhesion energy were deduced from a fit of Eq. (29) to the $c/a(\theta)$ data using the experimentally determined ratio, α_0, for each of the considered angular velocities (results of the fit are reported as solid lines in Fig. 6). The obtained effective adhesion energy is observed to increase with increasing angular velocity ($\Gamma=30$, 130 and 300 mJ m^{-2} for $\dot{\theta}=0.01$, 0.1 and 1 deg s^{-1}, respectively). These values are determined with a rather low accuracy, which may be related to the low adhesion energy of the fluorinated glass/PDMS couple chosen for this study. A more detailed description of viscoelastic dissipation at the crack tip remains to be done in this geometry, as it can be made in normal separation configuration [44].

Within the limit of nonadhesive stiction, the behavior of the stick region size as a function of the twist angle for any prescribed friction law is given by Eq. (12). Interestingly, it emerges from this expression that the orthoradial component of the interfacial stress should be zero at the center in order that there exists a finite angle θ_c

$$\theta_c = \lim_{c \to 0} \frac{1}{2\mu} \int_c^a \frac{\sigma_{\theta z}(\rho)}{\sqrt{\rho^2 - c^2}} d\rho, \qquad (32)$$

at which the stick region vanishes. Thus, this angle does not exist in the case for Coulomb or constant friction laws, as mentioned above. From a more mathematical point of view, the parity theorem for the polar coordinates (see [45], theorem 35, for example) also expresses that $\sigma_{\theta z}(r)$ has a simple zero at $r=0$. The question thus arises to define a friction law which exhibits this property for a twist experiment. The shear stress profiles obtained from the inversion of the displacement field [Fig. 7(g)] indicates that, in the vicinity of the contact center, the transition to a vanishing frictional stress at $r=0$ occurs over a length scale which is less than about 100 μm. In passing, it can be noted that a close examination of the early photoelastic results reported by Hetenyi and McDonald [15] also reveals some evidence of a vanishing shear stress at the center of torsional contacts, although this point was not commented by the authors. However, stress near the origin cannot be accurately calculated from the inversion procedure. Indeed, this length appears to be essentially dictated by the cut-off frequency associated with the deconvolution operation. In order to probe this effect, a calculated orthoradial displacement field was generated from the convolution of a constant orthoradial shear stress distribution ($\sigma_{\theta z}=0.2$ MPa, $r \leq a$) by the Green's function. Then, this displacement field was inverted using the iterative deconvolution algorithm in order to retrieve the initial shear stress distribution. For contact conditions close to the experimental ones, it can be seen (Fig. 10) that the de-

convolution operation is unable to retrieve the initial constant shear stress distribution at the vicinity of the contact center. The transition from $\sigma_{\theta z}=0$ at $r=0$ to $\sigma_{\theta z}=0.2$ MPa occurs within a region which size is similar to the experimentally determined one [Fig. 7(g)]. At this stage, one can therefore just conclude that the frictional shear stress under steady-state sliding vanishes at the center of the contact over a characteristic length which represents less than to 100 μm. Within this region, sliding paths are highly curved. The question thus arises to introduce a friction law for the local trajectory which depends on its curvature radius [50]. One may also argue that the velocity of the relative motion of both surfaces is reduced for the points which are near the center of the contact, leading to a zero friction stress when relative velocity is zero. Experimental results indicate that the frictional shear stress is only weakly velocity dependent down to 10 nm s^{-1} (Fig. 8). For the considered applied angular displacement rates such a threshold is typically achieved within less than one micrometer from the center of the contact. If any velocity dependence is involved in the vanishing shear stress at the center of the contact such an effect would therefore take place on a very short length scale.

In the above model, the size of the contact is kept constant during the whole stiction process in agreement with the experimental observation. On the other hand, it was mentioned in the introduction that stiction of rubbers under linear sliding conditions is often reported to involve a shrinkage of the contact area [10,12] which is attributed to the transition from the initial JKR adhesive contact to an Hertzian contact under frictional conditions [5,10,11]. For the investigated torsion configuration, a simple calculation shows that such a transition from a JKR to an Hertzian contact geometry would only result in a very limited reduction in the contact size. The adhesion energy of the PDMS/fluorinated glass system under investigation is not known, but $w=20$ mJ m^{-2} appears a reasonable upper bound value [46]. Using this value, the estimated reduction in the contact radius due to a transition from a JKR to an Hertzian contact (i.e., $w=0$) is found to be less than 4% for the considered contact conditions (normal load ≈ 0.3 N), i.e., close to the detection threshold. As a result, any shrinkage of the torsional contact due to the transition from JKR to Hertzian contact conditions would be barely detectable experimentally in our experiments.

One of the outputs of the contact model is the shear stress profile within the adhesive zone. As detailed in Appendix A, Eq. ((A8), $\sigma_{\theta z}(r)$ in the stick zone results from the addition of two terms (i) a sin^{-1} term corresponding to the nonadhesive contact situation (ii) an adhesive term involving the effective adhesion energy, Γ. In Fig. 11, the corresponding stress distribution has been reported together with experimental data. The theoretical calculations have been carried out for both the nonadhesive case ($\Gamma=0$) and for an adhesion energy, $\Gamma=200$ mJ m^{-2}, which corresponds to the upper bound of the experimental values (cf. above). It emerges that the experimental shear stress distribution within the adhesive zone is described quite satisfactorily by the adhesive model, which reflects the accuracy of the measurement.

V. CONCLUSION

Torsional friction data are obtained using an experimental setup where a sphere contacting an elastomer substrate is
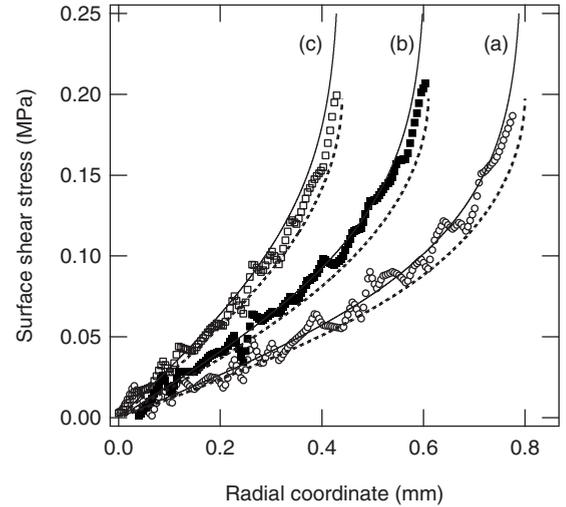
FIG. 11. Theoretical and experimental ($\dot{\theta}=1$ deg s^{-1}) surface shear stress profiles within the adhesive zone for two applied twist angles. (a) $\theta=0.21$ rad, (b) $\theta=0.27$ rad, and (c) $\theta=0.35$ rad The corresponding radii of the adhesive zone are 0.80 mm ($\theta=0.21$), 0.61 mm ($\theta=0.27$ rad), and 0.44 mm ($\theta=0.35$ rad). Theoretical stress profiles have been computed for a nonadhesive case ($\Gamma=0$, dashed line) and for $\Gamma=300$ mJ m^{-2} (solid line) using Eq. ((A8) and a frictional stress equal to 0.19 MPa.

rotating around its symmetry axis. It is shown that the steady-state friction regime is reached after a preliminary phase where microslip occurs in an annulus adjacent to the contact edge while a central contact disk remains in adhesive contact. In this stiction regime, the inner radius of the microslip annulus decreases until it invades the entire contact region. Using a previously developed inversion method, interfacial stress field during this preliminary phase is obtained. A model is proposed to describe this adhesion failure process in rotational symmetry. It relies on some adaptation of the well established Dugdale model for fracture which takes into account friction processes. Main experimental results are well described by the model. The torsional contact geometry is also shown to be well suited for the study of adhesion failure since the symmetry allows to consider this process as principally driven under a mode III fracture mechanics condition. Limitations of the description must be further analyzed. In particular, kinetics effects which are experimentally evidenced must be taken into account in order to more quantitatively interpret experiments. These effects are linked to a dependence of the interfacial friction stress on the sliding velocity and on potential viscoelastic dissipation within the rubber sample. Additional limitations may also arise from nonlinearities in the elastomer mechanical response, as some localized large deformations were achieved in the present experiments. Finally, some extension of the torsional contact experiment to the investigation of friction of viscoelastic substrate may be envisaged. In the steady sliding regime, bulk viscoelastic dissipation vanishes as no displacement takes place in the sample in the case of a single asperity contact. In such a situation, the velocity dependence of the measured interfacial stress must be attributed to interfacial dissipation only. By comparison, contacts with rough

spheres will reveal bulk viscoelastic dissipation effects. We believe that this approach will prove to be fruitful for analyzing both the adhesion failure processes and the steady sliding regime.

APPENDIX A: STRESS NEAR THE BOUNDARY OF THE STICK REGION

In the Dugdale-like presentation of the stiction, stress in the stick region can be expressed from Eq. (6)

$$\sigma_{\theta z}(r) = \frac{4\mu r}{\pi}\left[\int_r^c \frac{h_<(\alpha)}{\sqrt{\alpha^2 - r^2}}d\alpha + \int_c^{c^*}\frac{h_>^-(\alpha)}{\sqrt{\alpha^2 - r^2}}d\alpha \right.$$
$$\left. + \int_{c^*}^a \frac{h_>^+(\alpha)}{\sqrt{\alpha^2 - r^2}}d\alpha\right], \tag{A1}$$

where $h_<(\alpha)$, $h_>^-(\alpha)$, and $h_>^+(\alpha)$ are the derivative of $H_<(\alpha)$, $H_>^-(\alpha)$, and $H_>^+(\alpha)$. Noticing that $h_<(\alpha)=0$,

$$\sigma_{\theta z}(r) = \frac{2r}{\pi}\left[\int_c^{c^*}\frac{\tau_D - \tau_0}{\sqrt{c^{*2} - \alpha^2}}\frac{c^* d\alpha}{\alpha\sqrt{\alpha^2 - r^2}} \right.$$
$$\left. + \int_c^a \frac{\tau_0}{\sqrt{a^2 - \alpha^2}}\frac{ad\alpha}{\alpha\sqrt{\alpha^2 - r^2}}\right], \tag{A2}$$

$$= \frac{2}{\pi}\left[(\tau_D - \tau_0)\sin^{-1}\sqrt{\frac{c^{*2}/c^2 - 1}{c^{*2}/r^2 - 1}} + \tau_0\sin^{-1}\sqrt{\frac{a^2/c^2 - 1}{a^2/r^2 - 1}}\right], \tag{A3}$$

where relation (2.266) in [47] is used. One can verify that $\sigma_{\theta z}(r) = \tau_D$.

We will assume that the length of the Dugdale region, $c^* - c$ is small as compared to the radius c. Noting $\varepsilon = \frac{c^* - c}{c}$, the stress leading term can be written as

$$\sigma_{\theta z}(r) = \frac{2}{\pi}\left[(\tau_D - \tau_0)\frac{\sqrt{2\varepsilon}r}{\sqrt{c^2 - r^2}} + \tau_0\sin^{-1}\sqrt{\frac{a^2/c^2 - 1}{a^2/r^2 - 1}}\right]. \tag{A4}$$

The nondivergence condition reads:

$$2\theta = (\alpha_D - \alpha_0)\cosh^{-1}(1 + \varepsilon) + \alpha_0\cosh^{-1}\frac{a}{c}, \tag{A5}$$

then

$$\sqrt{2\varepsilon} \simeq \frac{2\theta - \alpha_0\cosh^{-1}\frac{a}{c}}{\alpha_D - \alpha_0}, \tag{A6}$$

$$\simeq \frac{\sqrt{\pi\mu\Gamma}}{(\tau_D - \tau_0)\sqrt{c}}, \tag{A7}$$

where Eq. (17) is used. Then, in the stick region

$$\sigma_{\theta z}(r) = \frac{2}{\pi}\left[\frac{\sqrt{\pi\mu\Gamma}}{\sqrt{c}}\frac{r}{\sqrt{c^2 - r^2}} + \tau_0\sin^{-1}\sqrt{\frac{a^2/c^2 - 1}{a^2/r^2 - 1}}\right]. \tag{A8}$$

Finally, near the edge of the stick region, $x \to 0^+$ (with $x = c - r$), stress behaves as

$$\sigma_{\theta z}(r) \simeq \sqrt{\frac{2\mu\Gamma}{\pi}}x^{-1/2}. \tag{A9}$$

By comparison with the definition [48]

$$\sigma_{\theta z}(r) \simeq \frac{K_{III}}{\sqrt{2\pi x}}, \tag{A10}$$

of the intensity factor for a mode III opening crack, one gets

$$K_{III} = 2\sqrt{\mu\Gamma}. \tag{A11}$$

For this opening mode, the elastic energy release rate reads

$$G = \frac{K_{III}^2}{4\mu}. \tag{A12}$$

Note that a factor of two is introduced as compared to a symmetrical crack opening, because one of the two media is not deformable [28]. One deduce

$$G = \Gamma, \tag{A13}$$

as expected from linear elastic fracture theory.

APPENDIX B: ACTUAL SLIDING VELOCITY AS A FUNCTION OF THE APPLIED TWIST ANGLE

In the partial friction regime, and in the sliding annulus $c^* < r < a$, displacements are obtained from Eq. (8) as

$$u_\theta(r) = -\frac{4}{\pi r}\left[\int_0^c \frac{\alpha^2 H_<(\alpha)}{\sqrt{r^2 - \alpha^2}}d\alpha + \int_c^{c^*}\frac{\alpha^2 H_>^-(\alpha)}{\sqrt{r^2 - \alpha^2}}d\alpha \right.$$
$$\left. + \int_{c^*}^a \frac{\alpha^2 H_>^+(\alpha)}{\sqrt{r^2 - \alpha^2}}d\alpha\right], \tag{B1}$$

where the expressions for $H_< = -\theta$, and $H_>^+$ and $H_>^-$ are given in Eqs. (18) and (20). Moreover, Eqs. (21) and (29) express, respectively, the continuity and the equilibrium conditions. For an angular velocity ω, the gap opening velocity between initially superimposed points on the substrate and on the lens at a radial distance r is

$$\frac{v}{\omega} = r - \frac{du_\theta(r)}{d\theta}.$$

In this expression, c, c^*, $H_<$, and $H_>^-$ depends on θ. Due to the continuity of the integrands the derivatives with respect to he boundaries of the integrals in Eq. (B1) cancel. After some algebra, an expression for the velocity as a function of the radius c can be found. Together with the equilibrium relation it gives a parametric expression of the velocity with respect to the rotation angle. Obtained expression is not reproduced here.

[1] C. Basire and C. Fretigny, Eur. Phys. J. A. **6**, 323 (1999).

[2] T. Goddenhenrich, S. Muller, and C. Heiden, Rev. Sci. Instrum. **65**, 2870 (1994).

[3] J. Israelachvili, *Fundamentals of Friction: Macroscopic and Microscopic Processes*, NATO Series (Kluwer, Dordrecht, 1992), Vol. 220, pp. 351–381.

[4] R. Mindlin, Trans. ASME, J. Appl. Mech. **16**, 259 (1949).

[5] K. L. Johnson, Proc. R. Soc. London, Ser. A **230**, 531 (1955).

[6] L. Bureau, C. Caroli, and T. Baumberger, Proc. R. Soc. London, Ser. A **459**, 2787 (2003).

[7] S. M. Rubinstein, G. Cohen, and J. Fineberg, Phys. Rev. Lett. **98**, 226103 (2007).

[8] S. M. Rubinstein, G. Cohen, and J. Fineberg, Phys. Rev. Lett. **96**, 256103 (2006).

[9] M. Barquins, Wear **158**, 87 (1992).

[10] M. Barquins, D. Maugis, and R. Courtel, C. R. Acad. Sci., Ser. IIb Mec. **280**, 49 (1975).

[11] A. Savkoor, Mechanical engineering dissertation, Technical University of Delft (1987).

[12] A. Savkoor and G. Briggs, Proc. R. Soc. Lond. A Math. Phys. Sci. **356**, 103 (1977).

[13] K. L. Johnson, Proc. R. Soc. London, Ser. A **453**, 163 (1997).

[14] A. Chateauminois and C. Fretigny, Eur. Phys. J. E **27**, 221 (2008).

[15] M. Hetenyi and P. McDonald, ASME Trans. J. Appl. Mech. **25**, 396 (1958).

[16] J. Lubkin, ASME Trans. J. Appl. Mech. **18**, 183 (1951).

[17] H. Deresiewicz, ASME Trans. J. Appl. Mech. **21**, 52 (1954).

[18] E. Dintwa, M. van Zeebroeck, E. Tijskens, and H. Ramon, Eur. Phys. J. B **39**, 77 (2004).

[19] E. Dintwa, M. V. Zeebroeck, E. Tijskens, and H. Ramon, Granular Matter **7**, 169 (2005).

[20] M. Barquins, R. Courtel, and D. Maugis, Wear **38**, 193 (1976).

[21] M. Chaudhury and J. Chung, Langmuir **23**, 8061 (2007).

[22] J. Liu, K. Kato, and K. Ohba, in *Proceedings of the International Tribology Conference (ITC'95)* (Han Lim Won Publishing Company, Korea, 1995).

[23] J. Liu, K. Ohba, K. Kato, and H. Inooka, Journal of the Visualization Society of Japan, Atlas of visualization **15**, 47 (1995).

[24] J. Scheibert, *Mécanique du Contact Aux Echelles Mésoscopiques., Sciences Mécaniques et Physiques* (Edilivres, Paris, France, 2008).

[25] J. Scheibert, G. Debrégeas, and A. Prevost, e-print arXiv:0809.3188.

[26] R. Bennewitz, J. David, C.-F. de Lannoy, B. Drevnlok, P. Hubbard-Davis, T. Mlura, and O. Trichtchenko, J. Phys.: Condens. Matter **20**, 015004 (2008).

[27] D. Maugis, J. Colloid Interface Sci. **150**, 243 (1992).

[28] D. Maugis and M. Barquins, J. Phys. D **16**, 1843 (1983).

[29] E. Gacoin, C. Fretigny, and A. Chateauminois, Tribol. Lett. **21**, 245 (2006).

[30] B. Briscoe and A. Chateauminois, Tribol. Int. **35**, 245 (2002).

[31] L. Landau and E. Lifshitz, *Theory of Elasticity*, 3rd ed. (Butterworth Heinemann, London, 1986).

[32] H. Bufler, Ing.-Arch. **27**, 137 (1959).

[33] J. Dundurs and D. Bogy, Trans. ASME, J. Appl. Mech. **36**, 650 (1969).

[34] K. Johnson, Langmuir **12**, 4510 (1996).

[35] J. Jager, Arch. Appl. Mech. **65**, 478 (1995).

[36] I. Sneddon, Int. J. Eng. Sci. **3**, 47 (1965).

[37] C. Basire and C. Fretigny, C. R. Acad. Sci., Ser. IIb Mec. **326**, 323 (1998).

[38] E. Barthel, J. Colloid Interface Sci. **200**, 7 (1998).

[39] K. Johnson and J. Greenwood, J. Colloid Interface Sci. **192**, 326 (1997).

[40] D. Hills and A. Sackfield, Trans. ASME, J. Appl. Mech. **53**, 372 (1986).

[41] F. Schneider, T. Fellner, J. Wilde, and U. Wallrabe, J. Micromech. Microeng. **18**, 065008 (2008).

[42] M. Deruelle, H. Hervet, G. Jandeau, and L. Léger, J. Adhes. Sci. Technol. **12**, 225 (1998).

[43] D. Maugis and M. Barquins, J. Phys. D **11**, 1989 (1978).

[44] E. Barthel and C. Fretigny, J. Phys. D **42**, 195302 (2009).

[45] J. Boyd, *Chebyshev and Fourier Spectral Methods*, 2nd ed. (Dover Publications, Inc., New York, 2000).

[46] M. Deruelle, M. Tirrell, Y. Marciano, H. Hervet, and L. Léger, Faraday Discuss. **98**, 55 (1994).

[47] I. Gradshteyn and I. Ryzhik, *Table of Integrals, Series and Products*, 4th ed. (Academic Press, New York, 1965).

[48] B. Lawn, *Fracture of Brittle Solids*, 2nd ed. (Cambridge University Press, Cambridge, 1993).

[49] A. Zmitrowicz, Int. J. Solids Struct. **43**, 4407 (2006).

[50] Such a curvature dependent friction has been analyzed [49] in a different context. In order to describe friction on nonhomogeneous or anisotropic surfaces, the author introduces component to the friction force which is perpendicular to the trajectory.